Final Draft

of the original manuscript

Examilioti, T.; Kashaev, N.; Enz, J.; Klusemann, B.; Alexopoulos, N.:
On the influence of laser beam welding parameters for autogenous AA2198 welded joints.
In: The International Journal of Advanced Manufacturing Technology. Vol. 110 (2020) 2079 - 2092.
First published online by Springer: 01.09.2020

https://dx.doi.org/10.1007/s00170-020-05893-8

On the influence of laser beam welding parameters for autogenous AA2198 welded joints

Theano N. EXAMILIOTI[a,b,c], Nikolai KASHAEV[a], Josephin ENZ[a], Benjamin KLUSEMANN[a,b] and Nikolaos D. ALEXOPOULOS[c1*]

[a] *Institute of Materials Research, Materials Mechanics, Helmholtz-Zentrum Geesthacht, D-21502 Geesthacht, Germany*

[b] *Institute of Product and Process Innovation, Leuphana University of Lüneburg, D-21335 Lüneburg, Germany*

[c] *University of the Aegean, School of Engineering, Department of Financial Engineering, 821 32 Chios, Greece*

Abstract

The effect of different autogenous laser beam welding process parameters on the fusion zone (FZ) geometry, microstructure and tensile mechanical properties were investigated for 5 mm thick AA2198 alloy sheets. Porosity formation and hot cracking are observed for low laser powers and welding velocities, while the porosity level is essentially reduced with increasing laser power. The characteristic cross-sectional geometry of the welded joints change with increasing laser power, taking shapes from narrow V-shape to rectangular I-shape and the results are discussed based on the 'closed' and 'open' keyhole formation during laser beam welding. A methodology is exploited in terms of quantifying the geometrical dimensions of the cross-section of the FZ in order to promote the welded joints with a narrow width as well as with a rectangular shape. The optimal process parameters, leading to FZ close to the desirable rectangular I-shape and with a low number of defects, are identified. Microstructural analyses reveal a pronounced transition zone in between the FZ and the heat-affected zone, which is subdivided into two narrow zones, the partially melted zone (PMZ) and the equiaxed zone. The narrow width of the FZ and PMZ, as well as the rectangular shape of the FZ, enable the autogenous welded joint to reach good tensile deformation properties.

Keywords: aluminum-lithium alloy; laser beam welding; AA2198; microhardness; tensile strength

1 Introduction

Third generation aluminum-copper-lithium (Al-Cu-Li) alloys are highly promising as they provide improved mechanical properties and damage tolerance behavior when compared to other aluminum-copper alloys **[1]**. Al-Cu-Li alloys were developed for lightweight and high-performance design and have already been used as structural materials for aerospace applications **[2]**. Innovative Al-Cu-Li alloys such as AA2198 and AA2196 provide low density, high specific strength, as well as better corrosion and fatigue crack growth resistance, compared to conventional Al-Cu alloys such as AA2024 **[3-5]**. The addition of lithium (Li) enables the formation of several strengthening precipitates depending on the Li content and heat

* Corresponding author: nalexop@aegean.gr

treatment conditions, besides the *S* type particles, also precipitates such as δ' (Al_3Li), δ (AlLi) and T_1 (Al_2CuLi) **[6]**. It is mentioned by Heinz et *al*. **[7]** and Lavernia and Grant **[8]** that the addition of 1 wt.% Li to Al reduces the density of the alloy by 3 % and the modulus of elasticity increases by almost 6 %.

Airframes are mainly joined with traditional techniques, e.g. riveting which is the state-of-the-art technology since 1920's for manufacturing aircraft structures **[9]**. In order to reduce manufacturing and materials costs and structural weight, the aerospace industries demand more efficient joining technologies. Exploiting the laser beam welding (LBW) process, Gialos et *al*. in **[10]** have shown that the total manufacturing cost can be reduced by up to 40 % and weight saving up to 28 %, can be reached when compared to traditional riveted structures. LBW is an efficient joining technique, which is already established in the aircraft industries for lower fuselage structures, e.g. **[11]**.

Nevertheless, Al-Cu-Li alloys exhibit several weldability problems when fusion welded. Hydrogen porosity, keyhole pores as well as hot-cracking are among the main problems of 2xxx aluminum series during LBW. Such problems in Al-Cu-Li alloys can be either partially avoided by employing different process welding parameters as mentioned by Chen and Gong **[12]** or by simply removing the surface oxidation layer according to Xiao and Zhang **[13]** before welding. Xiao and Zhang **[13]** showed that when removing 0.05 mm from the surface, essential increase in tensile elongation was noticed for LBW of an AL-Li 1420 alloy, due to the essential decrease in porosity. Recently, Enz et *al*. **[14]** showed that these defects can be essentially decreased by simply pre-heating the samples to be welded or by keeping the samples at an elevated temperature during the welding process. According to Kostrivas and Lippold in **[15]**, it is well known that these defects degrade the mechanical properties of the Al-Li welded joints. Other kind of geometrical weld defects, like underfill and root reinforcement can possibly reduce the mechanical properties, as shown by Kashaev et *al*. **[16]**. Lu et *al*. **[17]** demonstrated that the magnitude of the fusion zone (FZ) plays a significant role on the mechanical properties of the joint. Ahn et *al*. **[18]**, investigated the filler material feed rate and composition on the mechanical properties of fibre laser welded joints of AA2024-T3. It was concluded that the high feed rate produces instabilities, while the addition of filler metal itself reduces the risk of producing defects in the weld. Oliveira et *al*. in **[19]** also observed that the process parameters plays a significant role on the weld geometry, porosity and liquation cracking; in specific they concluded that the angle of the incident beam plays a pivotal role on porosity formation. Enz et *al*. in **[20]**, focused on the reduction of defects by employing different welding parameters without any filler material. Defect-free welds were achieved for large beam diameter by employing high defocusing and high laser power with a joint efficiency of around 69 %.

Investigations on the laser beam welding potential of Al-Li alloys can hardly be found in the literature; in most cases, a filler wire is used in order to reduce the defects in the weld seam, while sound welds can be produced with high joining efficiency. Zhang et *al*. **[21]** used the Al-12Si 4047 filler wire for LBW of AA2060 sheets. The ultimate tensile strength of the joints was around 80 % of that of the respective of the

base material. Liu et *al*. **[22]** performed LBW trials on the same Al-Li alloy with Al-5.6Cu filler wire to have a more compatible - by chemical composition - combination between the sheets to be welded and the filler wire. The exploitation of this filler wire gave V-shape welds, while the microstructure consisted mainly of θ' (Al_2Cu) and some S' (Al_2CuMg) precipitates. Han et *al*. in **[23]** performed LBW on T-joints between dissimilar alloys, e.g. AA2060/AA2099. They used two different filler wires, the typical 4047 wire and a new wire Al-6.2Cu-5.4Si with increased percentages of Cu and Si elements. It was found that the latter filler wire gave higher width equiaxed zones (EQZ) as well as low hot cracking formation. The main intergranular precipitate within the EQZ was T_2 (Al_5CuLi_3) from wire Al-6.2Cu-5.4Si filler wire unlike T (AlLiSi) noticed at the LBW joints with 4047 filler wire and strongly affects the hot cracking propagation. Zhang et *al*. **[24]** exploited the use of 5087 filler wire (Al with high Mg content), where AA2060 LBWed joints under optimized welding conditions were produced. Icosahedral phases (most likely to be T_2 phase with a stoichiometry of $Al_6Cu(Li,Mg)_3$) were found within the FZ and more specific along dendritic and grain boundaries. This filler wire gave defect-free welds; however, the joining efficiency was less than 65%.

Research on autogenous laser beam welded joints of Al-Li alloys is even more limited. Enz et *al*. **[14]** investigated the welding possibility of 3.2 mm sheet AA2198 with a Yb fibre laser. A joint efficiency of almost 57 % for the optimized autogenous welding parameters was obtained without any post-weld heat treatment that is in the same order of magnitude with the works of Wang et *al*. **[25]** and Ning et *al*. **[26]**. Malikov et *al*. **[27]** used a CO_2 laser to weld Al-Cu-Li (1421) alloy and obtained excellent mechanical properties with almost 90 % joint efficiency after the post-weld heat treatment (solid solution) of the welded joints. To this end, it is necessary to investigate the possibility of LBW without any filler wire (autogenous welding) in order to minimize chemical composition gradients in the FZ and therefore to increase the deformation capabilities of the welded joint.

In the present study, the Al-Li alloy 2198 was autogenously laser beam welded. The main goal of the present work is to identify the influence of the process parameters on the cross-sectional geometrical dimensions of AA2198 butt-welded joints. The focus lies on the production of welded joints with low level of structural defects and geometric imperfections so as to increase the tensile mechanical properties. The evolving microstructure and respective mechanical properties of the joint are investigated and compared against the available literature results.

2 Experimental procedure

The schematic overview about the experimental work of the present study is illustrated in **Figure 1**. Sheets from the aluminum alloy AA2198 material were autogenously laser beam welded by using different process parameters. Visual inspections as well as X-ray analysis were performed to assess systematically the weld quality. The cross-sections of the welds are characterized according to BS EN ISO 13919-2:2001 standard

with regard to their geometry (width, underfill, root reinforcement), microstructure as well as hardness measurements. The most suitable process parameters in this study are considered to be the ones that lead to a full penetration weld, absence of structural defects, high value of rectangular shape (I-shape) of the weld seam cross-section as well as low values of underfill and root reinforcement. Tensile specimens were machined from the welded sheet (**Figure 2**), produced with the most suitable process parameters, and tested according to ASTM E8 standard.

2.1 Material

Sheets of AA2198 in T3 heat treatment conditions with a nominal thickness of 5 mm are investigated. The chemical composition of AA2198 (supplied by Constellium) is given in **Table 1**. Sheets of 120 mm x 150 mm were machined parallel to the welding direction (**Figure 2**). Since, lithium increases typically the rate of the oxide film on the surface, which is responsible for the formation of porosity during welding **[28]**, the surface oxide film was removed before welding to avoid hydrogen porosity formation within the weld seam, i.e. mechanical milling of 0.2 mm for each side to be welded. All sheets were autogenously laser beam welded in 90° to the plate surface, see **Figure 2**.

2.2 Laser beam welding process

Laser beam welding was performed using a high-power ytterbium fibre laser (IPG YLS) with a maximum laser power of 8.0 kW. The characteristics of the used laser system are summarized in **Table 2.** Different laser process parameters were used, which resulted in different heat inputs. The exploited welding parameters in the present work are summarized in **Table 3**. In all experiments, Argon was used as shielding gas, which was delivered via the weld nozzle from the top and via the shielding gas path at the root side during welding of the butt joints, with gas flow of 15 1/min and 5.5 1/min, respectively. A high-accuracy, 6-axis industrial robot (KUKA KR 30HA) was used to move the laser optical system above the clamped specimens.

2.3 Welding quality and characterization of the welds

The quality of the welds was evaluated according to the procedures and requirements of the European standard BS EN ISO 13919-2:2001. Process parameters leading to welds that show incomplete penetration or macro-cracks were not examined further. Otherwise, non-destructive testing (NDT) methods, i.e. visual and radiographic analysis, and destructive testing (DT) methods were performed to examine the quality of the welds. Visual inspection was used to assess the surface condition of the weld seam. Attention was paid especially to imperfections such as excess of penetration, underfill (or incomplete filled groove), discontinuities and holes. Radiographic inspection was used according to EN ISO 17636-1 in order to determine the inner defects of the weld seams such as porosity and hot cracking.

Cross-sections were grounded with abrasive papers (SiC grits of 500, 800, 1200 and 2400 respectively), polished to a mirror finish with a 3 μm diamond suspensions and oxide polishing suspension compound (OP-S) and finally chemically etched by using Keller's reagent in order to improve the visibility of the microstructure. All microstructures were analyzed with a Leica DMI5000 M light optical microscope (LOM) and a scanning-electron microscopy (SEM) of type Jeol JSM-6490LV.

2.4 Mechanical testing

Microhardness measurements were carried out to evaluate the changes on the microstructure of the welded joint and especially at the heat-affected zone (HAZ) and the FZ, compared to the base material (BM). Vickers microhardness measurements were performed over the cross-sections of the welded joints according to DIN EN ISO 6507-1:2004 using a semi-automated Vickers microhardness testing machine (Shimadzu HMV-2000) with a test load of 1.96 N for 15 s. The measurements were conducted at room temperature and for three characteristic zones: (a) at the top line that was 750 μm below the radiation exposure side (RES); (b) at the middle line that was 2.300 μm from the top line and (c) at the bottom line that 750 μm above the weld root side (WRS), see **Figure 3**.

The tensile tests were conducted according to ASTM E8 specification on a Zwick Roell RM100 machine equipped with a 100 kN load cell. A Fiedler Opto-Electronic (FOE) laser extensometer WS-160-1005-AB was used to determine the deformation of the gauge length of the specimen during the tensile test with an accuracy of 0.01 mm.

3 Results and discussion

From the analysis of the weld joint cross-sections, it is observed that the main imperfections are incomplete fusion or incomplete penetration. The presence of such an imperfection, determines if the weld is classified as acceptable or non-acceptable. The results for the investigated process window in terms of laser power against welding velocity are summarized in **Figure 4**. The heat input is calculated as the fraction of laser power to welding velocity. The results show that the process window for obtaining full penetration is rather limited. For heat input values lower than 50 J/mm, no full penetration was achieved. To this end, all the produced welded joints with incomplete fusion were rejected for further optimization of the FZ geometry.

Lower welding velocities than 8.0 m/min are needed to fully penetrate the 5 mm thick sheets, which is correlated with the keyhole formation during welding. According to Krasnoperov et *al*. **[29],** there are two-keyhole penetration modes during laser beam welding: 'closed' and 'open' keyhole penetration mode. In the 'closed' keyhole penetration mode, the sheet is partially-to-full penetrated by a molten pool. The keyhole is not fully penetrating the thickness of the metal and therefore at the root of the weld there exists an area that is either not-melted (impartial fusion) or partially melted due to the reflections of the laser within the tunnel of the keyhole. According to Gao et *al*. **[30]**, this shape is called 'blind' keyhole and leads to either incomplete penetration, as seen for heat inputs larger than 50 J/mm in this study, or to V-shaped

geometries. This V-shape is justified since the upper part of the cross-section of the welded joint is well-formed by the keyhole formation; nevertheless, melting of the rest not-melted cross section of the joint (location near at bottom / root of the joint), is achieved by the heat input given by conduction from the upper, already molted part of cross-section of the joint. On the other hand, the 'open' keyhole mode is characterized by a formation, where the keyhole ends at the root of the weld and therefore is fully penetrating the thickness of the sheet. The laser beam is reflected within the keyhole and partially escapes through the bottom of the keyhole, and the melted material is prevented from over-heating. This enables to have narrow-width welds as well as of uniform thickness all over the thickness of the sheets to be welded. Hence, this kind of keyhole mode often leads to rectangular 'I' or 'H' shape welded joints.

3.1 Effect of processing parameters on joint geometry

3.1.1 Effect of laser power

In the present work, four different laser power energies are investigated, as presented in **Table 3**. Although porosity due to hydrogen in the surface oxide layer was avoided by milling before welding, for some parameter combinations macro-porosity can still be noticed on the images of the X-Ray inspection, **Figure 5**. For varying laser power at constant heat input, the radiographic analysis showed a high porosity formation at 5.0 kW. An increase in the laser power leads to a gradual decrease of the porosity level, nevertheless hot cracks appear, **Figure 5a**.

Xiao and Zhang in **[13]** reported that Al-Li alloys are sensitive to hot cracking due to their high thermal expansion and formation of eutectics during fusion welding. They stated that the susceptibility to hot cracking is affected from the solidification microstructure and is related to the contents of the alloying elements as well as of the welding parameters. It was mentioned that with increasing Li content there is an increased susceptibility for solidification cracking. Novikov and Grushko in **[31]** showed that increasing Li and Cu concentrations affect the hot cracking susceptibility (HCS). Similar, Han et *al*. **[32]** investigated the impact of Li chemical composition (wt.%) on the HCS, which showed that the sensitivity range of Li composition is located between 2.0 % and 3.0 % Li. Furthermore, the presence of Cu or Mg can reduce the HCS from 2 % to approximately 1 % Li. Moreover, hot cracking may also be promoted by pores; the latter can be further divided into metallurgical and keyhole pores, based on their size and shape. Keyhole pores have a round shape and are usually considered as hydrogen porosity. According to Xiao at *al*. in **[13]** and Whitaker et *al*. in **[33]**, the metallurgical porosity has an irregular shape (often spherical) and is usually formed at the weld root of the joint; it is often defined as unstable keyhole porosity. **Figure 6** shows exemplary the porosity formation for both cases: The welding conditions of 6 kW laser power and 70 J/mm heat input lead to metallurgical porosity, where for lower laser powers (e.g. 5 kW), irregular keyhole porosities is observed. Ahn et *al*. **[34]** reported that round macro-pores are generated due to keyhole collapse during welding which is attributed to large differences in melting and boiling points of the material. Lin et *al*. **[35]** numerically simulated several laser welded aluminum joints and showed that the violent melt flow

behind the keyhole is the root cause of pore formation. This leads to the collapse of the keyhole, which results in changes in the depth of the keyhole as well as to bubble formation.

In order to visualize the effect of the different laser powers and welding velocities on the geometrical shape of the weld seam, **Figure 6** shows the cross-sections of the laser beam welded joints. For lower laser powers, the weld seam presents a V-shape, where with increasing laser power the weld seam changes to an I-shape. As determined by Krasnoperov et *al*. in [**29**] the morphology of the cross-sectional profiles of the welded joints is mainly affected by the laser power and welding speed. It was observed that for high heat input the weld seam present similar width on the RES and WRS (I-shape), which is explained by the open keyhole mode, while for low heat input the width of the weld seam present a V-shape. Ehlen et *al*. **[36]** investigated the melt pool shape during laser welding and how it is influenced by Marangoni convection; they also observed V-shape characteristics for low laser powers. Examples of the V-shape morphology in the present study are observed for 7 kW and 70 J/mm or 6 kW and 60 J/mm, which is attributed to the 'closed' keyhole formation, where the laser beam is reflected within the keyhole and increases the width of the FZ. Similar V-shape weld cross-sections were also obtained in the article of Gao et *al*. in **[30]**. Additionally, they noticed that the I-shape welds present higher ultimate tensile strength than the respective welds with rectangular V-shape morphology at the cross-section due to the heterogeneities caused by LBW at the interface between FZ and base metal. Similar results were obtained by Lu et *al*. in **[17]**, where it is demonstrated that welds with rectangular I-shape (often called in the literature also as H-shape) result in higher tensile strength, when compared against respective V-shape joints, due to less strain gradients in the FZ/HAZ interphase and along the sheet thickness. Additionally, it is shown that welds with narrow I-shape give higher elongation at fracture when compared to wider I-shaped welds. Therefore, a rectangular I-shape of the weld seam can more efficiently distribute the strain field at the FZ/HAZ interface in order to increase at the macroscopic level the tensile mechanical properties of the weld.

Next to the geometrical characterization, the formation of underfill and root reinforcement imperfections was analyzed. For a laser power of 5 kW, significant underfill is noticed, and this underfill is maximum 0.40 mm in depth from the RES, **Figure 6**. According to ISO-13919 (stringent B), underfill values higher than 0.25 mm are considered as non-acceptable. The underfill formation is mainly associated with the evaporation and expulsion of liquid metal but also due to the gravity force of the fluid which flowed to the root of the weld. This geometrical effect induces more heat input to the material, widens the FZ and therefore allows the molten material to flow much easier and consequently geometries with high underfill can be noticed. Zhang et *al*. **[37]** also experienced simultaneously extreme underfill and root reinforcement in several welding trials. Geometries with high underfill, e.g. obtained by laser power of 5 kW, are accompanied by high root reinforcement imperfection, see **Figure 6**. By increasing the laser power the underfill as well as the accompanying root reinforcement gradually decrease up to 100 or even to 200 μm, which are considered as acceptable according to the stringent limits for imperfections for quality levels of ISO-13919.

3.1.2 Effect of welding velocity

In order to achieve defect-free welded joints, it is important to have an appropriate combination of the main laser beam welding parameters, like laser power and velocity. The welding velocity was chosen according to the estimation for each heat input parameter according to:

$$Welding\ Velocity\ [\text{mm/min}] = \frac{Laser\ Power\ [\text{kW}]}{Heat\ Input\ [\text{J/mm}]}, \quad (1)$$

The values of investigated heat input are based on the results of the preliminary tests as summarized in **Figure 4** and **Table 3**. To investigate the effect of laser power and welding velocity, X-Ray analysis are presented in **Figure 5b**. In the case of 60 J/mm heat input and 8 m/min welding velocity, several hot cracks are observed at low porosity. By increasing the heat input to 65 J/mm and decreasing welding velocity to 7.4 m/min, hot cracking still slightly increased but for the case of 70 J/mm heat input and 6.8 m/min welding velocity, hot cracking and porosity level decreased significantly. Likewise, Lin et *al*. **[35]** showed that the high welding velocity is beneficial in keeping the morphology of the 'open' keyhole and therefore not to create strong melt flow in laser welded aluminum joints.

3.1.3 Weld cross-section

Figure 6 shows the cross-sectional results from all welding parameters, in order to investigate the geometry and morphology of the weld seams in detail. The width of each weld seam was measured at different heights namely top, middle and bottom to calculate the width ratio of each cross-section. The first step focused on the identification of the weld shapes that are close to I-shape (rectangular). The 'width ratio' term is determined according to :

$$width\ ratio = \frac{W_{min}}{W_{max}}, \quad (2)$$

where w_{min} and w_{max} are the minimum and the maximum measured width from the three locations. The width ratio of the weld seam represents the FZ geometry, where a width ratio close or equal to one represents an I-shape (rectangular geometry), while lower values (of minimum 0.4 mm) represents a V-shape welded joint. **Figure 7** shows the width ratio results regarding heat input and laser beam power. The results show that for a low laser power of 5 kW, only V-shape welds are obtained. For the case of 6 kW laser power and for a high heat input, the width ratio gives a value of approximate 0.8 that corresponds to a shape close to rectangular and it was considered as appropriate for the second step evaluation of geometrical characterization of underfill and root reinforcement values. For the process parameter combination, involving a high laser power, i.e. 7 and 8 kW, almost rectangular FZ shapes form for low heat input values of 60 J/mm. Increase of the heat input for 7 kW laser power results in a V-shape geometry, with the weld width ratio taking values of around 0.6. For the maximum laser power of 8.0 kW and high heat input of 70 J/mm, the width ratio scored high values of approximately 0.7 to 0.8. Values of width ratio

of around 0.8 are among the maximum achieved. Width ratios of 0.4-0.6 represent geometries of V-shape and are therefore considered as geometrically non-appropriate.

The welded joints with high width ratio were further investigated in terms of underfill and root reinforcement, as presented in **Figure 8**. The results show that for the selected welding conditions, the geometrical 'defects' underfill (marked as *e*) and root reinforcement (marked as *f*) take values in between 0.4 and 0.8 mm. For the process parameter combination of 8.0 kW laser power and 6.8 m/min welding velocity, the evaluated 'geometrical' defects of underfill and root reinforcement take the lowest values out of all the investigated welds. Based on the characterization of the geometry of the fusion welds, this set of process parameters (8.0 kW laser power and 6.8 m/min welding velocity) represents the most rectangular shape of the FZ along with the minimum values of the geometrical defects in this study and, in this regard, was selected for further characterization in terms of microstructural analysis and mechanical properties.

3.2 Microstructural characterization

Figure 9a shows the microstructural morphology of the welding seam cross-section obtained by light optical microscopy for the LBW process performed with 8.0 kW laser power and 6.8 m/min welding velocity. Similar to other welded Al-Li alloys, a typical laser beam welded joint can be divided into four zones: FZ, transition zone (TZ), HAZ and BM, see **Figure 9b**. The TZ is located in between the FZ and HAZ and is divided into the partially melted zone (PMZ) and EQZ, with a fusion boundary in the middle. An EQZ can be seen in several Al-Li alloys, which is considered to be formed because of the lithium content in the material, e.g. Zhang et *al*. **[21]** and Ning et *al*. **[26]**. Several welding trials on Al-Li alloys with and without filler material and for different heat-inputs are summarized in **Table 4** regarding the PMZ and EQZ width of the welds. In the present experimental work, the total width of the PMZ and EQZ are within the range of 38 to 53 μm and are considered as narrow. In contrast, several welding investigations were performed by using different joining techniques, like gas metal arc welding (G-MAW) in 2A97 Al-Li alloy by Fu et *al*. **[38]**, fibre laser in AA2060 by Zhang et *al*. **[21]** and **[24]** as well as Nd:YAG laser and hybrid laser-arc welding in AA2198 by Faraji et *al*. **[39]**. In all cases, a large EQZ was obtained than the ones of the present article due to the different process parameters that were used. In several cases, the width of the TZ was more than double when compared to the results of the present work.

Equiaxed grains of 4 to 12 μm size are noticed in the EQZ, which is in good agreement with the available results from Fu et *al*. in **[38]**. The EQZ size slightly decreases in width from the radiation exposure side to the middle and then slightly increases to the weld root side. Han et *al*. **[23]** experienced that the EQZ has its maximum close to the radiation exposure side and decreases significantly close to the weld rood side. There it was also pointed out that the alloy element silicon plays a significant role on the EQZ width. Using an Al-Cu-Mg (CW3) filler wire instead of an AA4047 (Al-Si) filler wire, the EQZ width was more than halved. Fu et *al*. **[38]** observed that the width of the TZ (which includes EQZ and PMZ), is correlated with the changes of the laser beam welding parameters, e.g. laser power and heat input. The experimental results

agree well with results in the literature of the laser beam welding of AA2060 by Liu et *al*. in **[22]** as well as of 2A97 Al-Li alloy by Ning et *al*. **[26]** and Fu et *al*. **[38]**.

Microhardness mapping profiles at different heights of the cross-sections for the selected 'appropriate' welding parameters, i.e. 8.0 kW laser power and 6.8 m/min welding velocity, are presented in **Figure 10**. It can be seen that the microhardness in the FZ is much lower when compared to the BM. The hardness at the middle thickness of the weld cross-section present slightly lower values when compared to the top and the bottom measurements. The corresponding microstructure of the AA2198 weld is schematically illustrated in **Figure 11**, and it is considered to be valid for similar heat input values. For varying heat input values, differences in the size of the above district zones might appear. The BM is represented by the typical pancake-shaped grains due to the rolling manufacturing process. In the HAZ, the grain morphology represents the one of the BM, nevertheless, due to the heat input given, more precipitates are being formed as the material was welded in T3 condition that has low fraction of precipitates. According to Ning et *al*. **[26]** such precipitates are preferably needle-like T_1 precipitates (Al_2CuLi), θ' precipitates according to Liu et *al*. **[22]** or even horseshoe-shaped β' (Al_3Z_2) particles according to Wang et *al*. **[40]**. The PMZ consists of partially melted grains next to the HAZ and is in between the equiaxed zone (EQZ) with spherical equiaxed grains. The width of both zones is not uniform all over the welded joint, alike observed by Ning et *al*. **[26]** and is changing according to the welding process parameters. The width of such zones is reported in **Table 4** for various welding studies on Al-Li alloys in the literature. Similar grain structure morphology was noticed for several cases of Al-Li alloy welding, e.g. Zhang et *al*. **[21]**, Malikov et *al*. **[27]**.

From the experimental investigation of the present work as well as from the results of the relevant literature, it is clear that the shape of the FZ of Al-Li welded joints depends on the welding process and the addition not of a filler wire. The differences between these welding processes depend on the spot size being heated and the absorption by the plasma (CO_2 laser) or scattering by dust (fibre or YAG laser). The exploitation of fibre laser makes it easier to produce more narrow welds than CO_2 laser or even arc joints. Additionally, it is well known that the different welding process parameters increases the width of all zones, as can be seen in **Table 4** for different Al-Li welded joints.

During welding, the molten metal in the FZ is over-heated and therefore heterogeneous nucleation is the driving mechanism for solidification. Firstly, the liquid metal nucleates at the solid metal at the boundaries of the weld pool. In LBW, the low heat input and the high welding speed increase the ability of the weld metal to cool and therefore at the interface of solid/liquid, an EQZ forms. The width of EQZ changes according to the literature, as presented in **Table 4**. The crystals grow in the direction of main heat transfer, i.e. parallel to the grain structure of the sheet. Therefore, columnar dendrites are being formed on the both sides of the FZ of the welded joint. Shi et *al*. in **[41]** observed that in autogenous welds, large directionally oriented dendrites cannot be formed due to the high welding speed and the high convection velocity.

Finally, at the center of the melt pool, equiaxed dendrites are being formed, mainly because of the small temperature gradient present. This region (of high temperature) prevents the growth of columnar crystals

(solidification is not directional anymore) and therefore growth of equiaxed dendrites is noticed. This agrees with the results of Ning et *al*. in **[26]**, where the region of equiaxed dendritic structures comprised almost 80 % of the overall weld. Likewise, Liu et *al*. in **[22]** found coarse equiaxed grains with fully developed equiaxed dendrites in the center of the weld in LBW of AA2060 sheets.

3.3 Tensile test results

The obtained tensile results for an AA2198 BM specimen with 5 mm thickness for an autogenous laser beam welded specimen, welded with the previously identified most suitable process parameters, are presented in **Figure 12**. For comparison purpose, tensile results for BM and LBW specimens with 3.2 mm thickness are shown, which are taken from **[42]** and **[14]**, respectively. For 5 mm thick BM specimens, a high ultimate tensile strength of approximate R_m = 432 MPa and elongation at fracture of $A_T \approx 24$ % is determined. The BM specimens with 3.2 mm thickness, exhibited similar tensile mechanical performance with R_m = 448 MPa and A_T = 23 %.

The comparison between the BM and the autogenous laser welded specimens for 5 mm thickness shows a decrease in ultimate tensile strength and elongation at fracture. From the hardness measurements presented in **Figure 10**, it is clear that the FZ exhibits the lowest mechanical properties. The welded joints exhibit ultimate tensile strength values higher than 200 MPa (R_m = 215 MPa), while the elongation at fracture is approximately A_T = 4.7 %. Such value of the elongation at fracture is among the highest achieved for Al-Li alloys, as presented in **Table 4**. Comparing the elongation at fracture, is also evident that the autogenous welds achieved higher elongation at fracture values as with the addition of filler material.

The tensile results of autogenous laser welded AA2198-T3 joint of 3.2 mm was extracted from Enz et *al*. **[14]**. This specimen was tested in the as-welded condition (not milled) and therefore lower laser power value was exploited to weld the 3.2 mm thickness sheet. The optimal process parameters were identified to be 4 kW and 48 J/mm for laser power and welding velocity, respectively. Ultimate tensile strength R_m of the higher thickness sheet (5 mm) was slightly lower (11 %) than the lower thickness sheet (3.2 mm). Nevertheless, this slight difference in R_m was noticed in the BM of the two thicknesses. High difference in the elongation at fracture A_T was noticed for LBWed specimens, where the low thickness specimens exhibited values of approximate $A_T \sim 1.0$ % were recorded. This difference might be easily attributed to the differences in the process parameters that influence crack length, the shape and width of the FZ, etc. of the welded joint and as a result strongly influences the tensile mechanical behavior of the joint. This elementary, by means of tensile properties, comparison shows that the process parameters used in the present article allows for higher tensile ductility values of the welded joint.

3.4 Fractographical analysis

From the hardness measurements presented in **Figure 10**, it is clear that the FZ is the weakest zone of the joint. The interphases with the EQZ are usually the location of nucleating cracks of AA2198 welded joints,

as mentioned by Zhang et *al*. **[21]** and Fu et *al*. **[38]**, due to significant crystal misorientation in the boundary. In several cases, fracture initiates at locations with high stress concentration and propagates with a direction approximately 45 ^{o} to the tensile load axis and within the EQZ that acts as the interphase of the FZ to the HAZ of the welded joint. However, in contrast to literature results, where fracture occurred at the interphase between FZ and HAZ, the typical fracture location in the investigated autogenous laser beam welded joints is within the FZ, see **Figure 13a**. The fracture surface is approximately 45^{o} inclined to the tensile loading axis, showing evidence of ductile fracture. It can be noticed that when a groove cuts at the toe of the weld are missing from the FZ morphology, which are responsible for stress concentration at the specific locations. Fracture occurs firstly at the middle thickness due to either imperfections or high plastic strain and ends at geometrical defects like underfill and weld root. The findings of Dhondt et *al*. in **[43]** support the above concept, as they reported that high strength and low ductility mechanical properties are noticed at the mid-thickness of AA2050 alloy. Nevertheless, severe plastic deformation can be noticed in the above-mentioned locations of geometric imperfections, thus implying that fracture occurred at the latest stages of plastic deformation and therefore are not the sites where fracture was initiated. To this end, SEM analysis from the mid-cross section of the FZ reveals micro-porosity, **Figure 13b**, which may be the reason for the initiation of the micro-cracking mechanism. **Figure 13c** confirms this mechanism by illustrating secondary micro-cracking. The underlying mechanisms are consistent with the fracture mechanisms described by Ning et *al*. **[26]** in autogenous laser beam welded joints in 2A97 Al-Li alloy of 1.5 mm thick sheets.

As mentioned before, typically filler material is used in welding Al-Li alloys, see e.g. Liu et *al*. **[22]** and Fu et *al*. **[38]**. In most of the cases in the literature, the filler wire was rich in Si, Mg or Cu elements, which substantially increase the hardness in the FZ. To this end, the capability of the welded joint with filler wire for deformation are essentially low (< 1.6 % elongation at fracture). The comparison of elongation at fracture between welded joints with and without filler wire, shows that the autogenous welds can have almost three times the elongation at fracture (A_T ~ 4.5 % when compared to 1.6 % of the literature for welds with filler material).

4 Conclusion

In this investigation, sheets from Al-Cu-Li alloy AA2198-T3 were autogenously welded using a fibre laser and different welding process parameters. The main findings are summarized as follows:

1) Full penetration is achieved for autogenous laser beam welded process parameters of 5 mm thickness for higher heat inputs than 60 J/mm.
2) With increasing laser beam power up to 8 kW, porosity level is essentially reduced. However, hot cracks appeared for increasing laser power levels.
3) Geometrical defects such as underfill and root reinforcement are noticed for lower laser power and heat input. The fusion zone presents a narrow V-shape for lower laser power such as 6 kW, which is attributed to the 'closed' keyhole formation. With increasing laser power up to 8 kW the keyhole formation changes to 'open' that enabled to produce I-shape rectangular geometries of the welded seam cross-section.
4) Rectangular geometries are desirable according to the literature as these lead to higher mechanical properties of the welded joint. The optimal process parameters in terms of a rectangular I-shape of the fusion zone along with minimum underfill and root reinforcement are obtained at a laser power of 8.0 kW and at a welding velocity of 6.8 m/min.
5) Microstructural analyses show that equiaxed zone and partially melted zone are evident within the transition zone that acts as interphase with the heat-affected zone at the fusion zone. The equiaxed zone in the present study is found to be very narrow when compared to the literature and plays a significant role for the ability of the welded joint in achieving good tensile mechanical properties.
6) Fracture surface analysis shows that failure initiated from the micro-pores formation in the middle of the cross-section of the welded joint. Micro-cracking is noticed, and fracture surface was 45^{o} inclined to the load axis showing evident of ductile fracture with elongation at fracture exceeding 4.5 %.

5 References

[1] Dursun T, Soutis C. Recent developments in advanced aircraft aluminum alloys. Mater Des 2014;56:862-871. https://doi.org/10.1016/j.matdes.2013.12.002.

[2] Rioja RJ, Liu J. The evolution of Al-Li base products for aerospace and space applications. Metall Mater Trans A 2012;43:3325-3337. https://doi.org/10.1007/s11661-012-1155-z.

[3] Pantelakis SG, Alexopoulos ND. Assessment of the ability of conventional and advanced wrought aluminum alloys for mechanical performance in light-weight applications. Mater Des 2008;29:80-91. https://doi.org/10.1016/j.matdes.2006.12.004.

[4] Alexopoulos ND, Migklis E, Stylianos A, Myriounis DP. Fatigue behavior of the aeronautical Al–Li (2198) aluminum alloy under constant amplitude loading. Int J Fatigue 2013;56:95-105. https://doi.org/10.1016/j.ijfatigue.2013.07.009.

[5] Alexopoulos ND, Proiou A, Dietzel W, Blawert C, Heitmann V, Zheludkevich M, Kourkoulis SK. Mechanical properties degradation of (Al-Cu-Li) 2198 alloy due to corrosion exposure. Procedia Struct Integrity 2016;2:597-603. https://doi.org/10.1016/j.prostr.2016.06.077.

[6] Yoshimura R, Konno TJ, Abe E, Hiragaa K. Transmission electron microscopy study of the evolution of precipitates in aged Al–Li–Cu alloys: the θ′ and T1 phases. Acta Mater 2003;51:4251-4266. https://doi.org/10.1016/S1359-6454(03)00253-2.

[7] Heinz A, Haszler A, Keidel C, Moldenhauer S, Benedictus R, Miller WS. Recent development in aluminium alloys for aerospace applications. Mater Sci Eng A 2000;280:102-107. https://doi.org/10.1016/S0921-5093(99)00674-7.

[8] Lavernia EJ, Grant NJ. Aluminium-lithium alloys. J Mater Sci 1987;122:1521-1529. https://doi.org/10.1007/BF01132370.

[9] Starke EA, Staley JT. Application of modern aluminum alloys to aircraft. Prog Aerosp Sci 1996;32:131-172. https://doi.org/10.1016/0376-0421(95)00004-6.

[10] Gialos AA, Zeimpekis V, Alexopoulos ND, Kashaev N, Riekehr S, Karanika A. Investigating the impact of sustainability in the production of aeronautical subscale components. J Clean Prod 2018;176:785-799. https://doi.org/10.1016/j.jclepro.2017.12.151.

[11] Dittrich D, Standfuss J, Liebscher J, Brenner B, Beyer E. Laser Beam Welding of Hard to Weld Al Alloys for Regional Aircraft Fuselage Design–First Results. Phys Procedia 2011;12:113-122. https://doi.org/10.1016/j.phpro.2011.03.015.

[12] Chen L, Gong S. The research on YAG laser welding porosity of Al-Li alloy. Adv Mater Res 2011;287-290:2175-2180. https://doi.org/10.4028/www.scientific.net/AMR.287-290.2175.

[13] Xiao R, Zhang X. Problems and issues in laser beam welding of aluminum-lithium alloys. J Manuf Process 2014;16:166-175. https://doi.org/10.1016/j.jmapro.2013.10.005.

[14] Enz J, Carrarin C, Riekehr S, Ventzke V, Kashaev N. Hot cracking behavior of an autogenously laser welded Al-Cu-Li alloy. Int J Adv Manuf Tech 2018;95:299-310. https://doi.org/10.1007/s00170-017-1197-x.

[15] Kostrivas A, Lippold JC. Weldability of Li-bearing Aluminium Alloys. Int Mater Rev 1999;44:217-237. https://doi.org/10.1179/095066099101528289.

[16] Kashaev N, Ventzke V, Çam G. Prospects of laser beam welding and friction stir welding processes for aluminum airframe structural applications. J Manuf Process 2018;36:571-600. https://doi.org/10.1016/j.jmapro.2018.10.005.

[17] Lu G, Zhang L, Pie Y, Ning J, Zhang J. Study on the size effects of H-Shaped fusion zone of fiber laser welded AZ31 joint. Metals 2018;8:198-212. https://doi.org/10.3390/met8040198.

[18] Ahn J, Chen L, He E, Davies CM, Dear JP. Effect of filler feed rate and composition on microstructure and mechanical properties of fibre laser welded AA2024-T3. J Manuf Process 2017;25:26-36. https://doi.org/10.1016/j.jmapro.2016.10.006.

[19] Oliveira PI, Costa JM, Loureiro A. Effect of laser beam welding parameters on morphology and strength of dissimilar AA2024/AA7075 T-joints. J Manuf Process 2018;35:149-160. https://doi.org/10.1016/j.jmapro.2018.08.003.

[20] Enz J, Riekehr S, Ventzke V, Huber N, Kashaev N. Fiber laser welding of high-alloyed Al-Zn-Mg-Cu alloys. J Mater Process Technol 2016;237:155-162. https://doi.org/10.1016/j.jmatprotec.2016.06.002.

[21] Zhang X, Huang T, Yang W, Xiao R, Liu Z, Li L. Microstructure and mechanical properties of laser beam-welded AA2060 Al-Li alloy. J Mater Process Technol 2016;237:301-308. https://doi.org/10.1016/j.jmatprotec.2016.06.021.

[22] Liu F, Wang X, Zhou B, Huang C, Lyu F. Corrosion Resistance of 2060 Aluminum–Lithium Alloy LBW Welds Filled with Al-5.6Cu Wire. Materials-Basel 2018;11:1988. https://doi.org/10.3390/ma11101988.

[23] Han B, Tao W, Chen Y, Li H. Double-sided laser beam welded T-joints for aluminum-lithium alloy aircraft fuselage panels: effects of filler elements on microstructure and mechanical properties. Opt Laser Technol 2017;93:99-108. https://doi.org/10.1016/j.optlastec.2017.02.004.

[24] Zhang X, Yang W, Xiao R. Microstructure and mechanical properties of laser beam welded Al-Li alloy 2060 with Al-Mg filler wire. Mater Des 2015;88:446-450. https://doi.org/10.1016/j.matdes.2015.08.144.

[25] Wang X, Lu F, Wang HP, Qu Z, Xia L. Micro-scale model based study of solidification cracking formation mechanism in Al fiber laser welds. J Mater Process Technol 2016;231:18–26. https://doi.org/10.1016/j.jmatprotec.2015.12.006.

[26] Ning J, Zhang L, Bai Q, Yin X, Niu J, Zhang J. Comparison of the microstructure and mechanical performance of 2A97 Al-Li alloy joints between autogenous and non-autogenous laser welding. Mater Des 2017;120:144-156. https://doi.org/10.1016/j.matdes.2017.02.003.

[27] Malikov A, Orishich A, Golyshev A, Karpov E. Manufacturing of high-strength laser welded joints of an industrial aluminum alloy of system Al-Cu-Li by means of post heat treatment. J Manuf Process 2019;41:101-110. https://doi.org/10.1016/j.jmapro.2019.03.037.

[28] Tian Y, Robson JD, Riekehr S, Kashaev N, Wang L, Lowe T, Karanika A. Process Optimization of Dual-Laser Beam Welding of Advanced Al-Li Alloys Through Hot Cracking Susceptibility Modeling. Metall Mater Trans A 2016;157:3533-3544. https://doi.org/10.1007/s11661-016-3509-4.

[29] Krasnoperov MY, Pieters RRGM, Richardson IM. Weld pool geometry during keyhole laser welding of thin steel sheets. Sci Technol Weld Join 2014;9:501-506. https://doi.org/10.1179/136217104225021733.

[30] Gao XL, Zhang LJ, Liu J, Zhang JX. Effect of weld cross-section profiles and microstructure on properties of pulsed Nd:YAG laser welding of Ti6Al4V sheet. Int J Adv Manuf Technol 2014;72:895-903. https://doi.org/10.1007/s00170-014-5722-x.

[31] Novikov II, Grushko OE. Hot cracking susceptibility of Al–Cu–Li and Al–Cu–Li–Mn alloys. J Mater Sci Technol 1995;11(9):926-932. https://doi.org/10.1179/mst.1995.11.9.926.

[32] Han J, Wang J, Zhang M, Niu K. Susceptibility of lithium containing aluminum alloys to cracking during solidification. Materialia 2019;5:100203. https://doi.org/10.1016/j.mtla.2018.100203.

[33] Whitaker IR, McCartney DG, Calder N, Steen WM. Microstructural characterization of CO2 laser welds in the Al-Li based alloy 8090. J Mater Sci 1993;28:5469–5478. https://doi.org/10.1007/BF00367817.

[34] Ahn J, Chen L, He E, Dear JP, Davies CM. Optimisation of process parameters and weld shape of high power Yb-fibre laser welded 2024-T3 aluminium alloy. J Manuf Process 2018;34:70-85. https://doi.org/10.1016/j.jmapro.2018.05.028.

[35] Lin R, Wang HP, Lu F, Solomon J, Carlson BE. Numerical study of keyhole dynamics and keyhole-induced porosity formation in remote laser welding of Al alloys. Int J Heat Mass Tran 2017;108:244-256. https://doi.org/10.1016/j.ijheatmasstransfer.2016.12.019.

[36] Ehlen, G, Ludwig A, Sahm, PR. Simulation of time-dependent pool shape during laser spot welding: transient effects. Metall Mater Trans A 2003;34:2947-2961. https://doi.org/10.1007/s11661-003-0194-x.

[37] Zhang M, Chen G, Zhou Y, Liao S. Optimization of deep penetration laser welding of thick stainless steel with a 10 kW fiber laser. Mater Des 2014;53:568-576. https://doi.org/10.1016/j.matdes.2013.06.066.

[38] Fu B, Qin G, Meng X, Ji Y, Zou Y, Lei Z. Microstructure and mechanical properties of newly developed aluminum-lithium alloy 2A97 welded by fiber laser. Mater Sci Eng A 2014;617:1-11. https://doi.org/10.1016/j.msea.2014.08.038.

[39] Faraji AH, Moradi M, Goodarzi M, Colucci P, Maletta C. An investigation on capability of hybrid Nd:YAG laser-TIG welding technology for AA2198 Al-Li alloy. Opt Laser Eng 2017;96:1-6. https://doi.org/10.1016/j.optlaseng.2017.04.004.

[40] Wang S, Huang Y, Zhao L. Effects of different aging treatments on the microstructures and mechanical properties of Al-Cu-Li alloy joints welded by electron beam welding. Chinese J Aeronaut 2018;31:363-369. https://doi.org/10.1016/j.cja.2017.07.002.

[41] Shi Y, Zhong F, Li X, Gong S, Chen L. Effect of laser beam welding on tear toughness of a 1420 aluminum alloy thin sheet. Mater Sci Eng A 2007;465:153-159. https://doi.org/10.1016/j.msea.2007.02.079.

[42] Examilioti TN, Klusemann B, Kashaev N, Riekehr S, Enz J, Alexopoulos ND. Anisotropy and size effect in tensile mechanical properties of AL-Cu-Li 2198 alloy. Procedia Struct Integrity 2017;5:13-18. https://doi.org/10.1016/j.prostr.2017.07.052.

[43] Dhondt M, Aubert I, Saintier N, Olive JM. Mechanical behavior of periodical microstructure induced by friction stir welding on Al–Cu–Li 2050 alloy. Mater Sci Eng A 2015;644:69-75. https://doi.org/10.1016/j.msea.2015.05.072.

List of figures

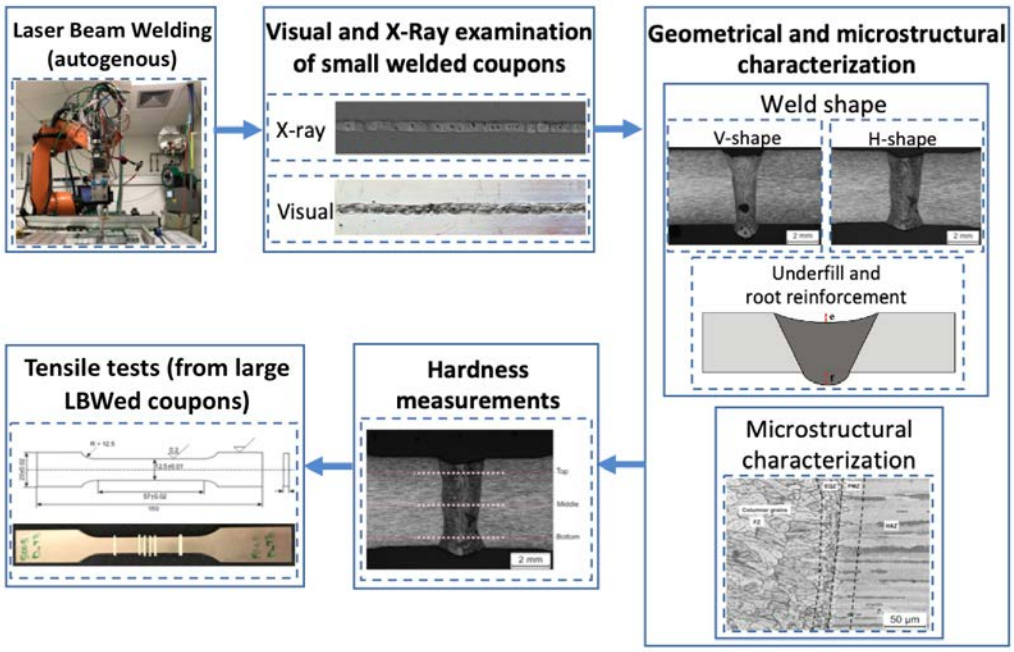

Figure 1: Schematic overview about the performed study.

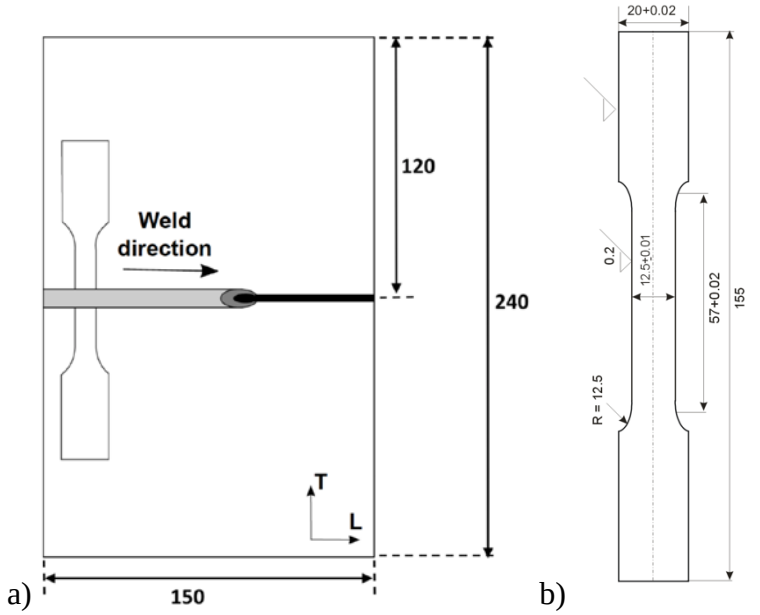

Figure 2: a) Direction of the welding seam and b) standard tensile specimen configuration according to ASTM E8. All dimensions are in mm.

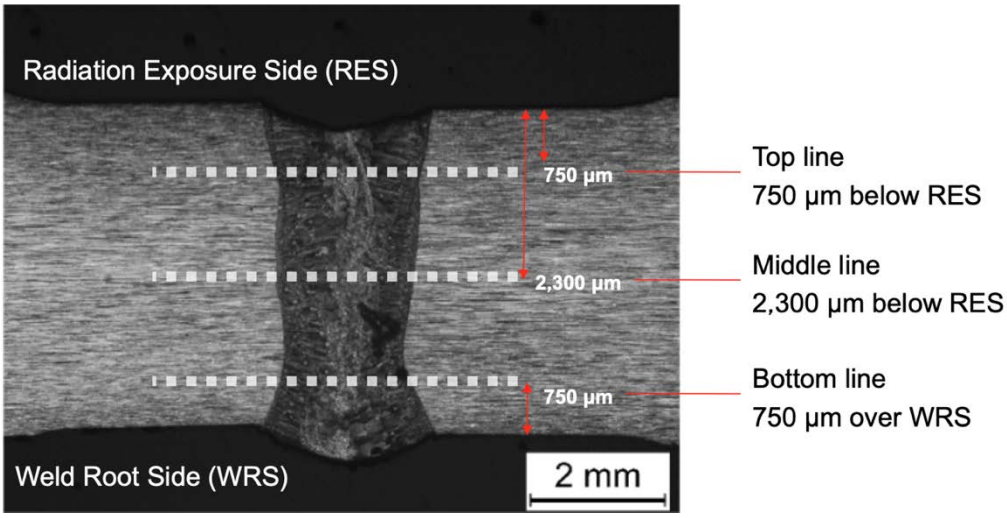

Figure 3: Example of the location profiles for the microhardness measurements in the cross-section of the welded joint.

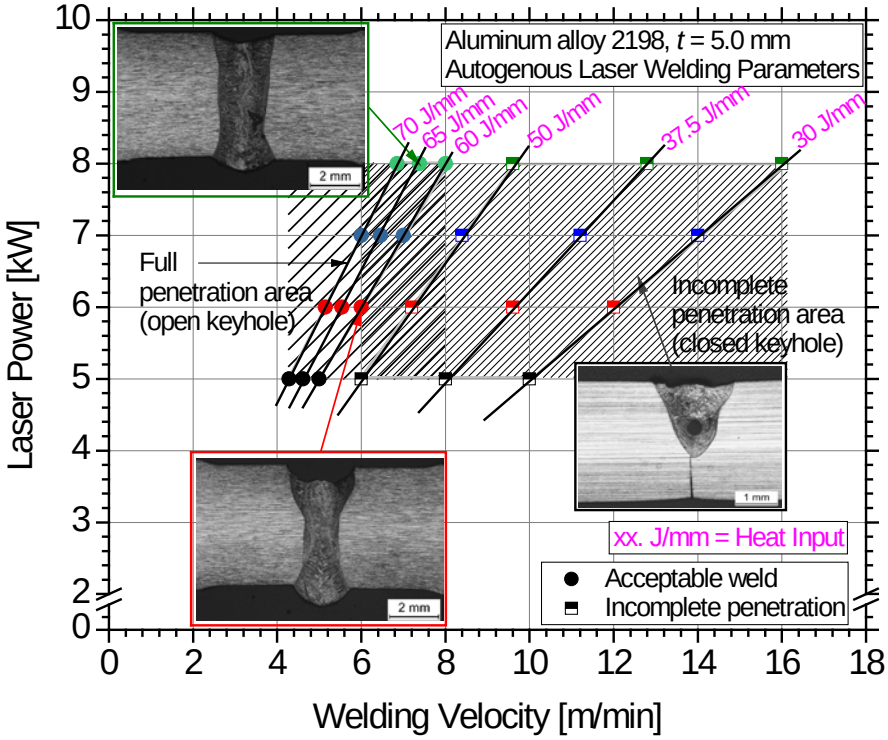

Figure 4: Laser beam welding process window for the investigated material.

a)

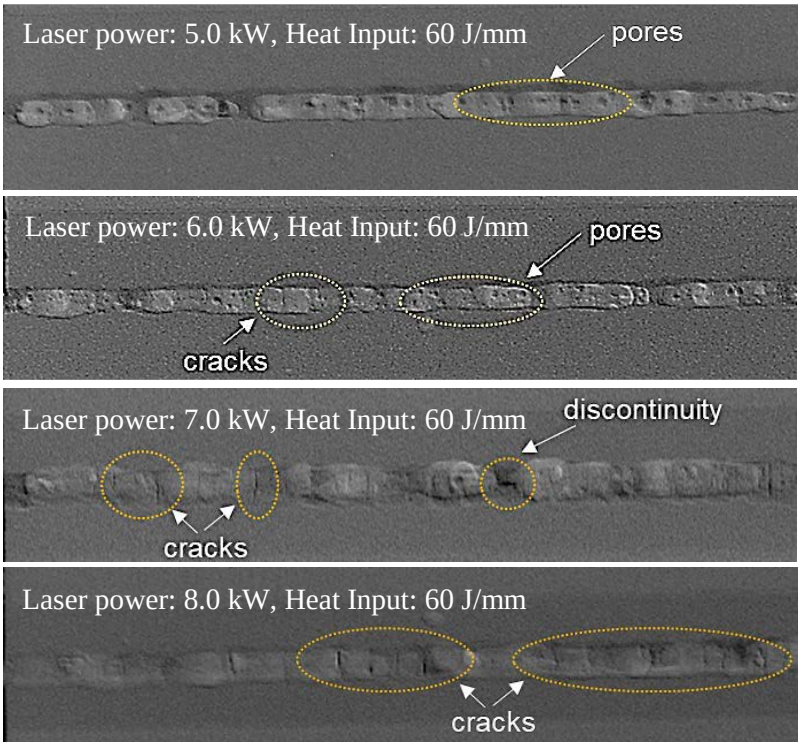

b)

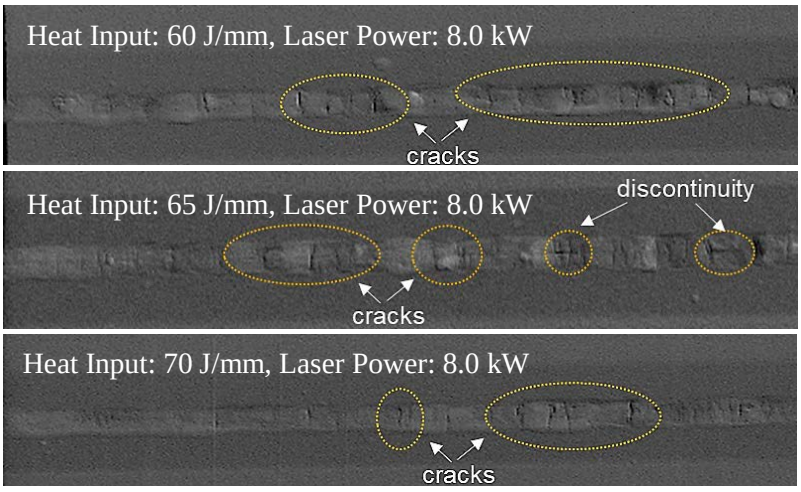

Figure 5: Radiographs for different welds produced with constant a) heat input of 60 J/mm and b) laser power of 8.0 kW.

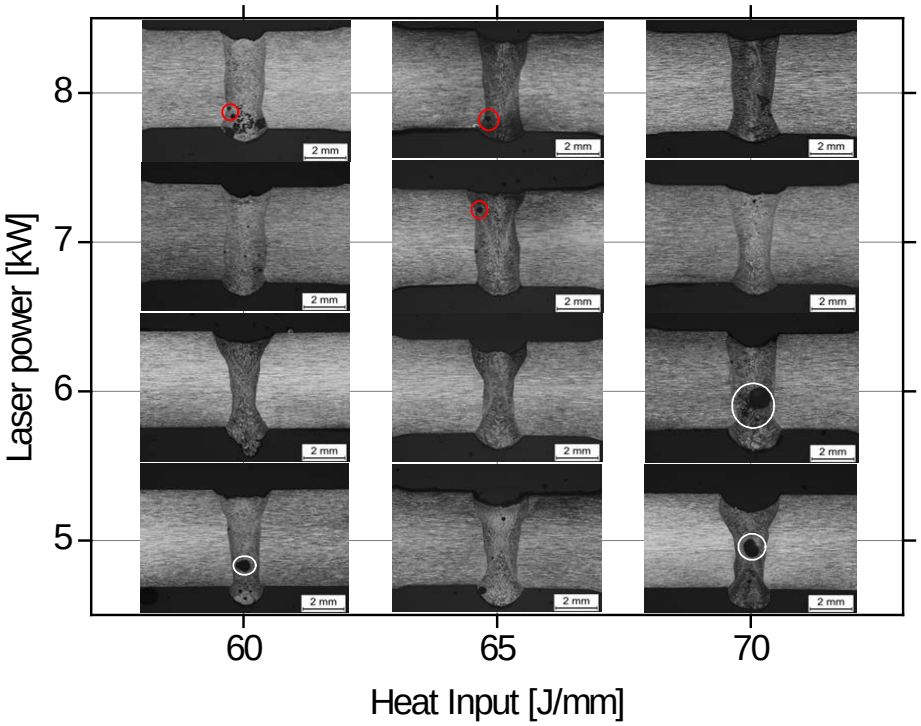

Figure 6: Cross-sections of the welded joints of the main welding parameters, i.e. heat input and laser power. Irregular keyhole porosities are presented with white circles and round shape porosity with red circles.

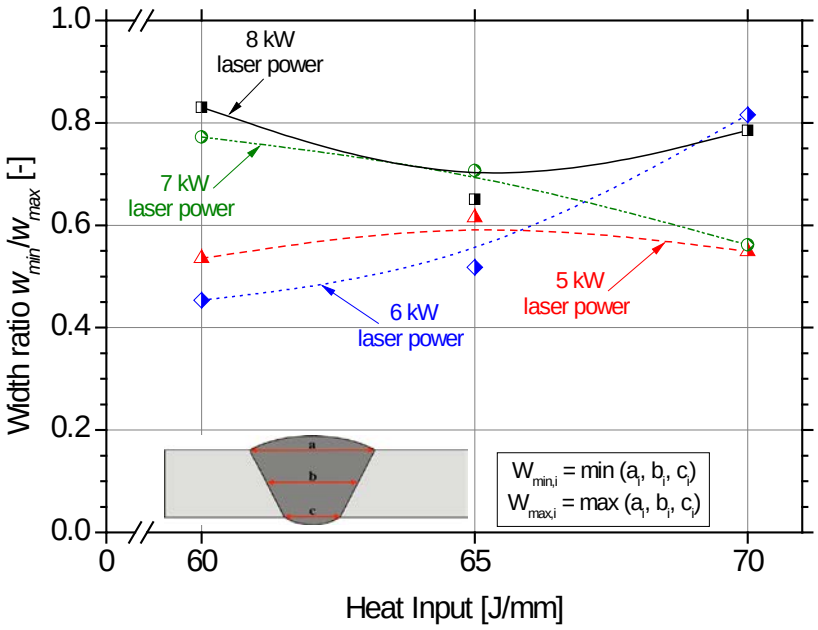

Figure 7: Schematic representation of width ratio of the cross-section of the welded joints with different heat input and laser power. The available test results were simply fitted with the aid of B-spline curve in order to roughly assess the effect of each parameter.

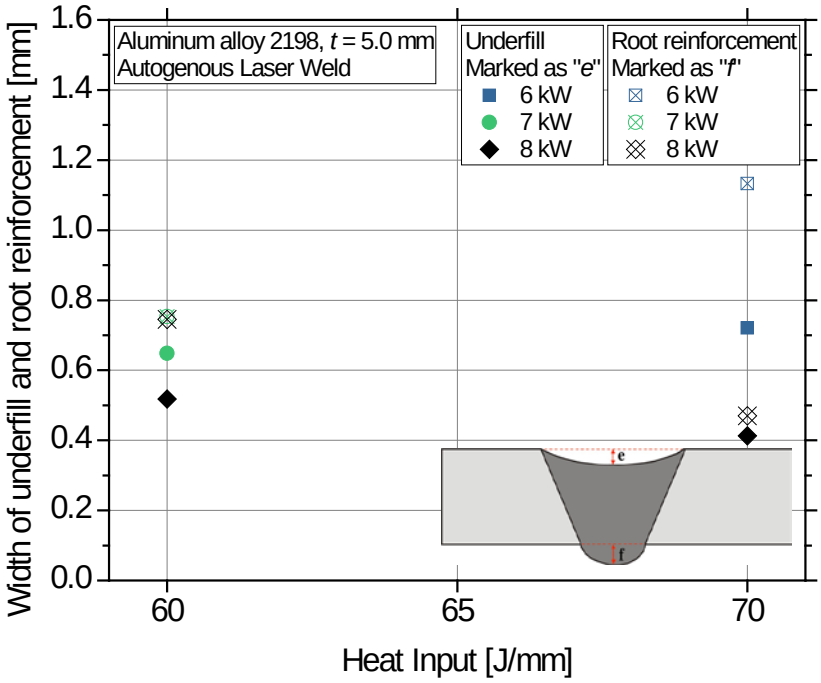

Figure 8: Schematic representation of the underfill *e* and root reinforcement *f* of the cross-section of the welded joints with the higher width ratio.

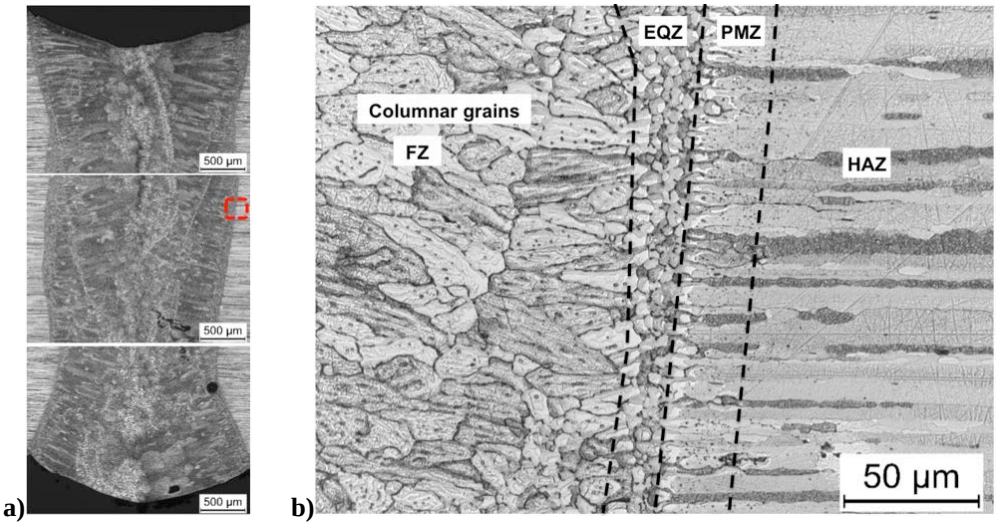

Figure 9: a) Macrograph of the cross-section of the weld with 8.0 kW laser power and 6.8 m/min welding velocity, which represent the optimal process parameters according to the present study. b) Micrograph, showing the discrete zones at the fusion boundary.

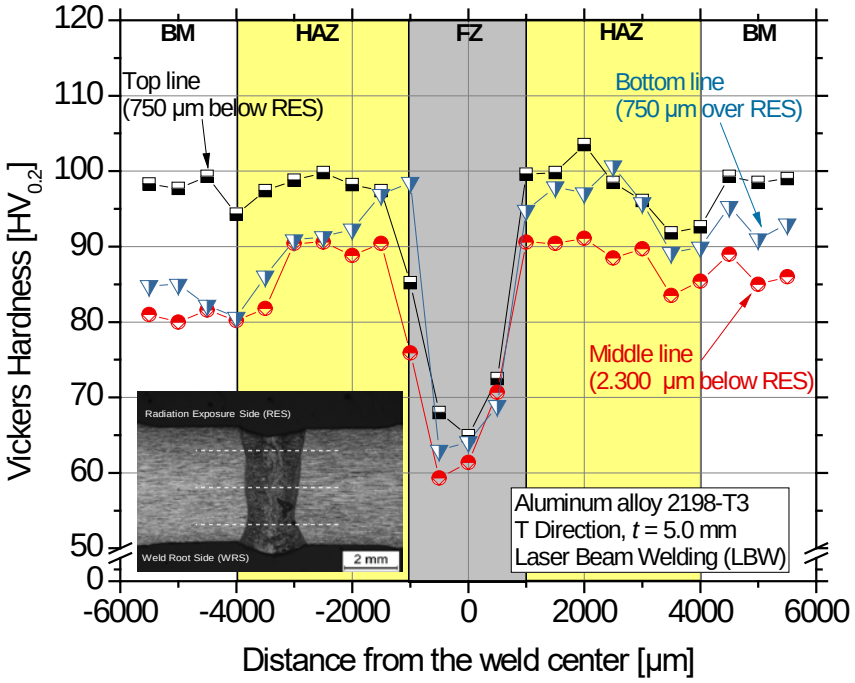

Figure 10: Microhardness profiles of the autogenous laser beam welded AA2198-T3 joint, welded with 8.0 kW laser power and 6.8 m/min welding velocity.

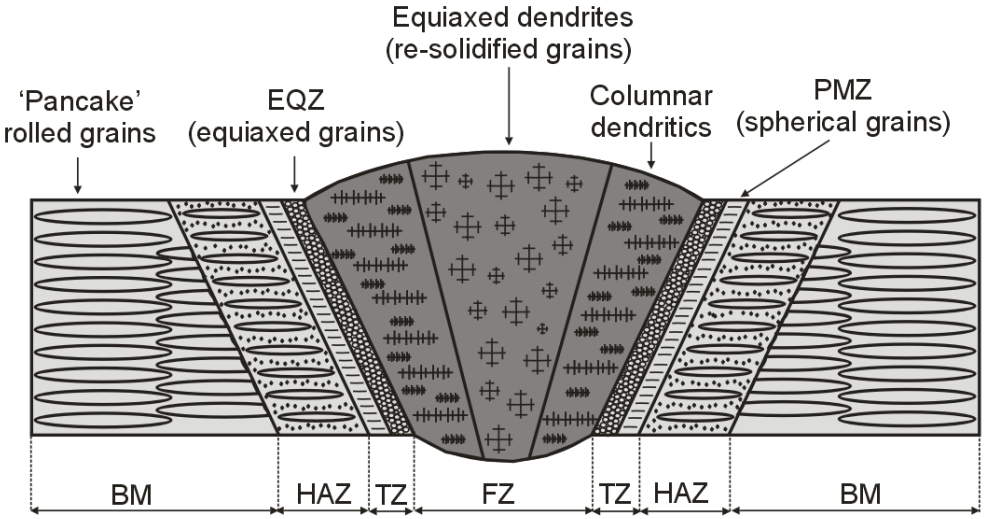

Figure 11: Microstructure model diagram of face-to-face laser beam welded joint of AA2198 sheets.

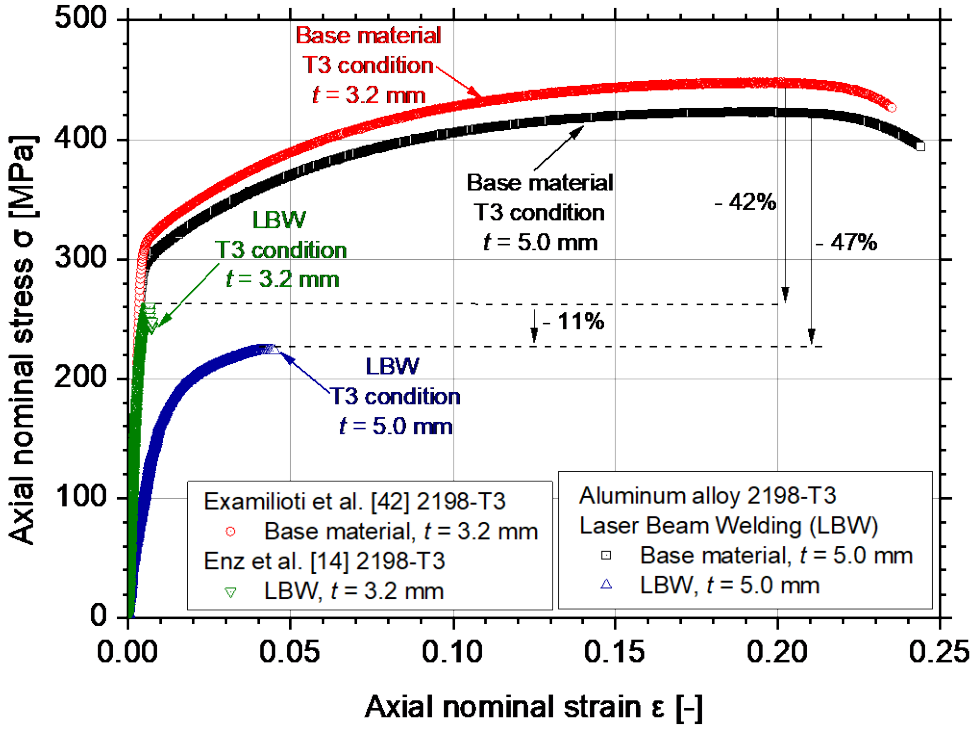

Figure 12: Tensile (nominal) stress-strain results of the laser beam welded aluminum alloy 2198 joint and base material. For comparison purpose, literature results for lower thickness are shown as well.

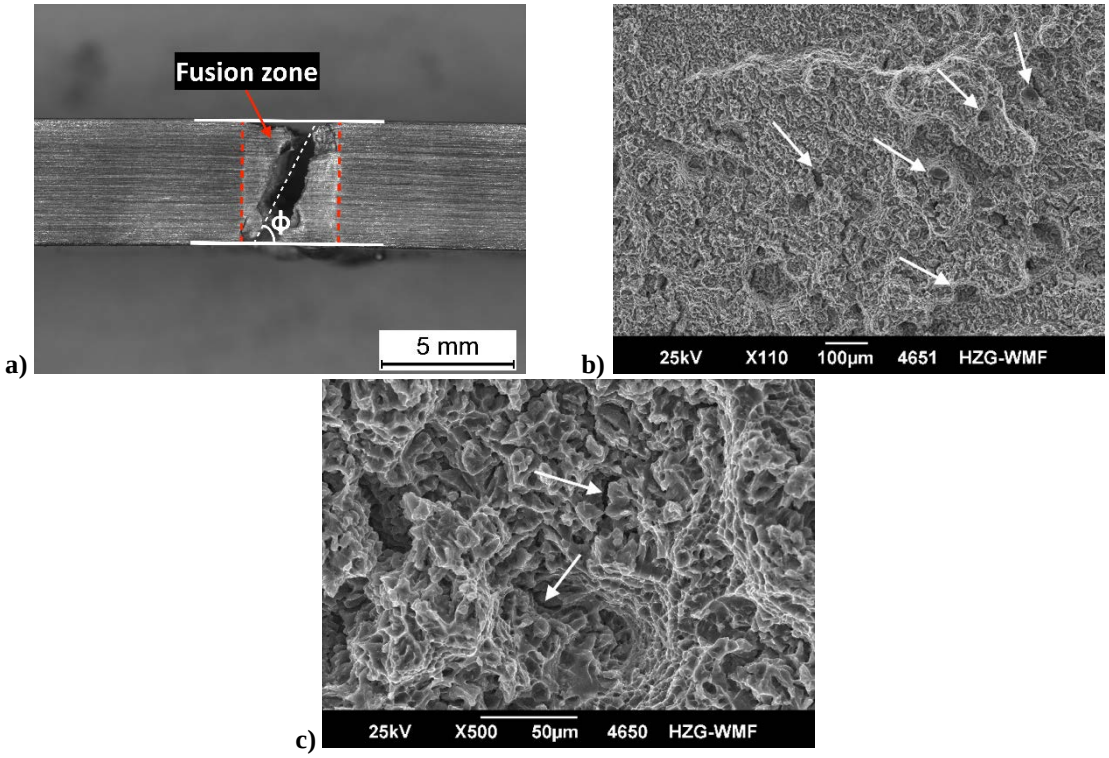

Figure 13: Micrographs of a) cross-section failure location with angle φ, b) and c) fractrographs obtained via SEM analysis from the mid-cross section of autogenous laser beam welded joints of AA2198.

6 List of Tables

Table 1: Chemical composition of aluminum alloy AA2198 supplied by Constellium (in wt.%).

Alloy	Si	Fe	Cu	Mn	Mg	Li	Zn	Zr	Ag	Ti	Al
AA2198	0.03	0.05	3.35	0.1	0.32	0.99	0.1	0.14	0.27	0.30	Bal.

Table 2: Characteristics of fibre laser used in this study.

Property	Yb fibre laser
Maximum power [kW]	8.0
Focal position [mm]	0.0
Wavelength [µm]	1.07
Beam parameter product [mm × mrad]	7.5
Fibre diameter [µm]	200
Focal length [mm]	300
Collimator length [mm]	120
Laser spot diameter (in focus) [µm]	512
Rayleigh length [mm]	8.784
Irradiance distribution	top-hat

Table 3: Process parameters used for autogenous laser-beam welding.

No.	Laser power [kW]	Welding velocity [m/min]	Heat input [J/mm]
Parameters resulted in incomplete penetration			
1	5	10	30
2	6	12	30
3	7	14	30
4	8	16	30
5	5	8	37.5
6	6	9.6	37.5
7	7	11.2	37.5
8	8	12.8	37.5
9	5	6	50
10	6	7.2	50
11	7	8.4	50
12	8	9.6	50
Parameters resulted in full penetration			
13	5	5	60
14	6	6	60
15	7	7	60
16	8	8	60
17	5	4.6	65
18	6	5.5	65
19	7	6.5	65
20	8	7.4	65
21	5	4.3	70
22	6	5.1	70
23	7	6	70
24	8	6.8	70

Table 4: Butt-welding concepts on Al-Li alloys with fibre laser beam welding (LBW)**, quantification of the equiaxed (EQZ) and partially melted (PMZ) zones of the weld seam cross-section and respective estimated tensile elongation at fracture values.**

Article	Base material [thickness] / Filler material	Heat Input	EQZ	PMZ	Estimated elongation at fracture
Zhang et al. **[21]**	AA2060-T8 [2.0 mm] / AA4047	-	40-120 µm	40-50 µm	1.2 %
Liu et al. **[22]**	AA2060 [2.0 mm] / ER2319	42 J/mm	20 µm	-	-
Han et al. **[23]**	AA2060-T8-AA2099 (T-joint) [2.0 mm] / AA4047	18 J/mm	67-77 µm	-	1.7 %
Han et al. **[23]**	AA2060-T8-AA2099 (T-joint) [2.0 mm] / CW3 (Al-6.2%Cu-5.4%Si)	18 J/mm	33 µm	-	3.8 %
Zhang et al. **[24]**	AA2060-T8 [2.0 mm] / AA5087	90 J/mm	30-60 µm	-	~ 1.6 %
Ning et al. **[26]**	AA2A97-T3 [1.5 mm] / autogenously	24 J/mm	5-11 µm	5-7 µm	~ 1.8 %
Ning et al. **[26]**	AA2A97-T3 [1.5 mm] / AA2319	-	25-50 µm	25-140 µm	~ 2.3 %
Fu et al. **[38]**	AA2A97 [2.0 mm] / autogenously	-	30-90 µm	-	~ 4.7 %
Faraji et al. **[39]**	AA2198 [3.0 mm] / autogenously *	-	50-100 µm	250-300 µm	-
Wang et al. **[40]**	Al-Cu-Li-T8 [4.0 mm] / autogenously +	-	20 µm	-	4.5 %
Present experimental work	AA2198-T3 [5.0 mm] / autogenously	70 J/mm	20 – 30 µm	25 µm	4.7 %

* *Hybrid Nd:YAG LBW and TIG welding*

+ *Electron beam welding (EBW)*